Modeling and inverse design of bio-inspired multi-segment pneu-net soft manipulators for 3D trajectory motion

Cite as: Appl. Phys. Rev. **8**, 041416 (2021); https://doi.org/10.1063/5.0054468
Submitted: 19 April 2021 • Accepted: 05 November 2021 • Published Online: 21 December 2021

Chengru Jiang, Dong Wang, Baowen Zhao, et al.

Modeling and inverse design of bio-inspired multi-segment pneu-net soft manipulators for 3D trajectory motion

Cite as: Appl. Phys. Rev. **8**, 041416 (2021); doi: 10.1063/5.0054468
Submitted: 19 April 2021 · Accepted: 5 November 2021 ·
Published Online: 21 December 2021

View Online Export Citation CrossMark

Chengru Jiang, Dong Wang,[a] Baowen Zhao, Zhongkun Liao, and Guoying Gu[a]

AFFILIATIONS

The Robotics Institute and State Key Laboratory of Mechanical System and Vibration, School of Mechanical Engineering, Shanghai Jiao Tong University, Shanghai, 200240, China

[a]Authors to whom correspondence should be addressed: wang_dong@sjtu.edu.cn and guguoying@sjtu.edu.cn

ABSTRACT

A biological organism, such as an octopus tentacle or elephant trunk, exhibits complex 3D spatial trajectories. Although soft manipulators showing 2D in-plane deformations have been extensively studied and applied in many areas, the design method of soft manipulators with a mathematical model that can follow a particular 3D spatial trajectory remains elusive. In this paper, we present a methodology to automatically design bio-inspired multi-segment pneu-net soft manipulators that can match complex 3D trajectories upon single pressurization. The 3D motions can be characterized by a combination of twisting, bending, and helical deformations, which are enabled by the design of the soft segments with programmable chamber orientations. To inverse design the soft manipulators with trajectory matching, we develop an analytical framework that takes into account the material nonlinearity, geometric anisotropy, and varying loading directions. The spatial trajectory can be reconstructed by combining with a 3D rod theory. In this sense, multi-segment soft manipulators with trajectory matching are inversely designed by varying the geometric and material parameters. We further demonstrate the grasping of complex objects using the designed soft manipulators. The proposed methodology has immense potential to design soft manipulators in 3D space and broaden their application.

I. INTRODUCTION

Biological organisms that can exhibit 3D spatial motions are ubiquitous in nature. Examples include bacteria flagella for locomotion,[1] plant tendrils for climbing,[2] and elephant trunks for grasping.[3] Inspired by nature, many soft manipulators are developed to mimic the complex motion of animals and match specific trajectories,[4–7] which introduce promising potentials in various applications, such as implantable and wearable devices,[8–11] robots moving through unpredictable terrains,[12,13] and gripper grasping objects of unknown geometry.[14,15]

Although there has been significant progress of soft manipulators owing to the inherent compliance, easy fabrication, and ability to achieve complex output motions from a simple input, the advancement of this field is hindered by numerous challenges, such as dynamic models, modeling contact, and modeling designs with multiple actuators and hyper redundancy. However, these challenges are difficult to address, as soft robotics is still in its early stage. Therefore, much research currently focuses on the more fundamental problem: how to design the soft manipulators for a particular 3D trajectory motion using a single actuation based on the mathematical modeling. To this end, researchers have made efforts to develop and model soft manipulators.

A typical example is the McKibben actuators, which consist of an elastomeric tube wrapped in inextensible fibers and show 1D elongation or contraction.[16–19] To broaden the applications of soft manipulators, many soft manipulators exhibiting 2D in-plane motions are developed,[14,20,21] such as starfish grippers;[22] soft tentacles;[23] tethered and untethered quadruped walkers;[24,25] tripedal jumping robots;[26] soft gloves,[27] etc. Several models have been proposed to model the 2D motions of the soft manipulators. For example, a model based on Euler's theory of the elastica is proposed for pneu-net soft actuators, and the shape and curvature of the bending deformation are well captured.[28] A theoretical model for pneu-net soft actuators is proposed based on the friction laws, which can be used to control the motion and maximize the displacement of the soft robot along a prescribed direction.[29] The bending behaviors of soft fiber-reinforced actuators are investigated.[30]

Although soft manipulators have allowed for various innovative applications, there is an urgent need for design methods to efficiently and systematically design manipulators following complex 3D trajectories. This area is still in its infancy, and several studies have been conducted to show how to form complex deformations using a single actuation.[31–33] While soft manipulators showing 2D in-plane deformations have been extensively studied, the design method of soft manipulators with an analytical model that can follow a particular 3D spatial trajectory remains elusive. Previous models of the 3D soft manipulators mainly focus on fiber-reinforced soft manipulators.[34,35] For example, Connolly *et al.* developed an analytical model for fiber-reinforced soft manipulators that exhibits bending, twisting, elongation, and expansion motions.[33] Gong *et al.* presented soft manipulators with an opposite-bending-and-stretching structure for efficient underwater spatial grasping.[36]

In addition to the diverse functions exhibited by fiber-reinforced soft manipulators, pneu-net soft manipulators can also demonstrate complex 3D trajectories by adjusting the chamber distributions. Compared to the complicated fabrication procedures and the complex combinations of fibers of the fiber-reinforced soft manipulators, the pneu-net soft manipulators are easier to be made and the arrangements of chambers are more flexible. Thus, sophisticated 3D trajectories can be created using pneu-net soft manipulators with simpler structures, but the design of the pneu-net soft manipulators with 3D trajectory matching is hindered, mainly due to the lack of appropriate modeling approaches that take into account the material nonlinearity, geometric anisotropy and spatial actuation. Although several approaches were proposed to study the 3D motions,[37–41] most of them are based on the finite element method (FE). While the results produced by FE models are interesting and compelling, they are challenging to generate tractable models and inverse design. There are a few design methods for pneu-net soft manipulators that can match specific trajectories with a combination of the bending, twisting and helical deformations in 3D space. Developing analytical models is desirable for control algorithms and understanding the design parameters for soft robots.

Inspired by the octopus tentacles where a single tentacle can exhibit complex 3D trajectories [Fig. 1(a)], we propose a new design of pneu-net soft manipulators that can match complicated trajectories in 3D space. The soft manipulator consists of multiple segments [Fig. 1(b)], where each segment shows a different actuation mode: twisting, in-plane bending, or helical actuation. By combining different segments, the soft manipulators can exhibit various spatial trajectories under single input pressure. The bending and helical segments consist of angled chambers on one side of the soft manipulator, whereas the twisting segment consists of two sets of aligned chambers on both sides. By tuning the angles of the chambers, a wide range of twisting, bending, or helical shapes can be achieved.

To facilitate the design of 3D multi-segment pneu-net soft manipulator with trajectory matching, a theoretical framework is developed to build the relationship between the manipulator's deformation and its geometrical, material, and loading parameters. A nonlinear model based on a phenomenological orthotropic energy density function is used to model the twisting segment, which considers the material nonlinearity and geometric anisotropy. We employ a minimum potential energy method to model the multiple helical segment soft manipulators. The deformed shape is then reconstructed using a 3D rod theory, and a method is developed to visualize the deformed shape. By virtue of the low computational cost, various 3D trajectories are designed by varying the geometric, material and loading parameters. It also enables the inverse design of bio-inspired soft manipulators that follow specific trajectories. The developed method contains the following two main novel contributions: (1) we propose the design of a pneu-net twisting segment and develop a nonlinear model to describe its actuation; (2) we propose an inverse design method to design the soft manipulator's 3D spatial trajectories by adjusting the geometric parameters.

This paper is organized in the following manner. The theoretical model for the soft manipulators is presented in Sec. II and validated by

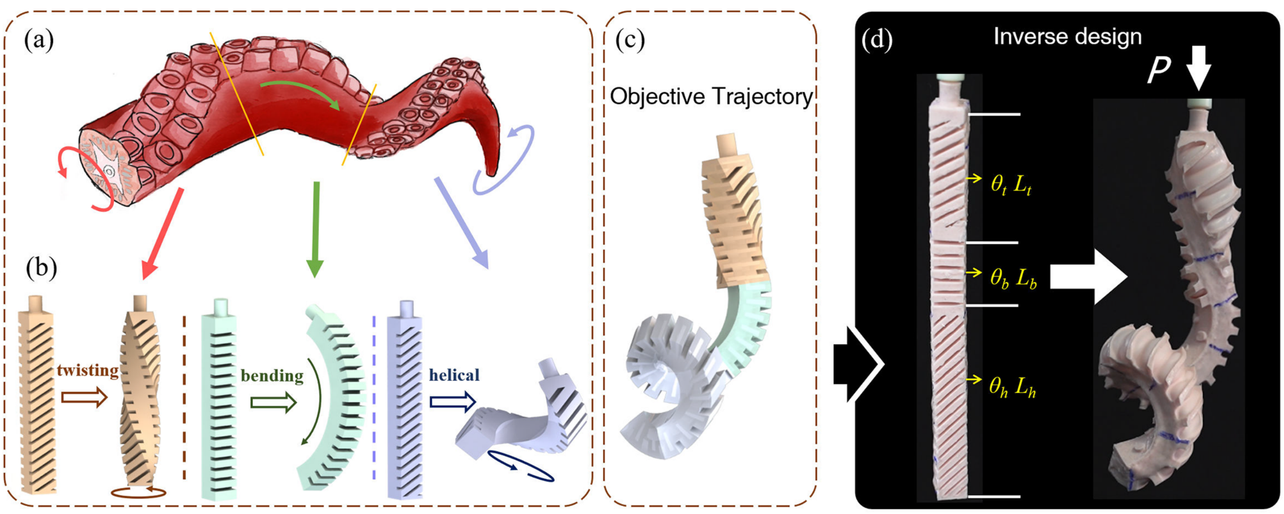

FIG. 1. Designing a bio-inspired multi-segment soft manipulator that replicates a complex 3D spatial trajectory. (a) A single octopus tentacle's motion can be characterized by a combination of twisting, bending and helical deformation. (b) Inspired by the octopus tentacle, soft segments showing twisting, bending and helical deformations are designed by programming chamber orientations. (c) Shows the schematic of a 3D objective trajectory. (d) Using the design methodology, the geometric, material, and loading parameters for each segment are output for replicating the objective trajectory.

experiments and FE simulations in Sec. III. Various multi-segment soft manipulators are designed in Sec. IV. Conclusions are given in Sec. V.

II. THEORETICAL MODEL FOR MULTI-SEGMENT SOFT MANIPULATORS

The schematic of a multi-segment soft manipulator is presented in Fig. 2(a). We denote each segment's length and orientation angle as $L^{(i)}$ and $\theta^{(i)}$, where $i = 1$ to N. N is the number of segments. Each segment can be a twisting, bending or helical segment. The centerline of the deformed multi-segment soft manipulator is represented by a space curve $\boldsymbol{P}(s)$, where $\boldsymbol{P}$ represents the global coordinate of each point on the deformed arc length s. S represents the original arc length. To characterize the shape of the soft manipulator, a global coordinate $(\boldsymbol{X}_1, \boldsymbol{X}_2, \boldsymbol{X}_3)$ and an orthonormal local coordinate $(\boldsymbol{x}_1, \boldsymbol{x}_2, \boldsymbol{x}_3)$ are used, as sketched in Fig. 2(a). Both coordinates move along the centerline. $\boldsymbol{x}_1$ is identified as the tangent vector of the centerline. $\boldsymbol{x}_2$ and $\boldsymbol{x}_3$ lie along the width and height directions. The theoretical model for a single twisting segment is derived next. The theoretical model for the helical segment is given in Sec. I of the SI. In both models, the gravity is neglected.

A. Theoretical model for twisting segment

The energy density function of the twisting segment is obtained first. The relationship between the deformation of the twisting segment and the input pressure is established next.

1. Energy density function of the twisting segment

As shown in Fig. 2(b)(i), the twisting segment consists of two sets of aligned chambers with the same angles on both sides. An internal channel connects the arranged chambers, as shown by the cross-section in Fig. 2(b)(iii). From the experimental observation, we find that the amount of twisting in the cross-section is uniform and the centerline of the deformed twisting segment remains straight. No obvious warping is observed. Based on the above observations, the irregular cross-section is simplified to an axisymmetric cross-section to ease the derivation of analytical solutions, as shown in Fig. 2(b)(iv). The inner and outer radii R_i and R_o are obtained by equating the inner empty area and the occupied area between the original and simplified cross sections. As shown later, the analytical deformed twisting shapes obtained agree well with the experiments.

A nonlinear phenomenological model is used for the twisting segment. The inner layer is isotropic, while the outer layer is anisotropic due to the aligned chambers. The energy density function of the twisting soft actuator is then the sum of the two parts:

$$W_t = c_1 W_t^{iso} + c_2 W_t^{aniso}, \tag{1}$$

where $c_1 = 0.27$ and $c_2 = 0.73$ are the volume fractions of the isotropic and anisotropic parts, respectively. W_t^{iso} and W_t^{aniso} are the energy density functions of the isotropic and anisotropic parts. For the isotropic inner part, we choose a simple incompressible neo-Hookean model,[33]

$$W_t^{iso} = \frac{\mu}{2}(I_1 - 3), \tag{2}$$

where $\mu = 0.317$ MPa denoting the shear modulus and $I_1 = tr(\boldsymbol{F}\boldsymbol{F}^T)$. $\boldsymbol{F}$ is the deformation gradient.

For the orthotropic outer layer, the following energy density function is used:[42]

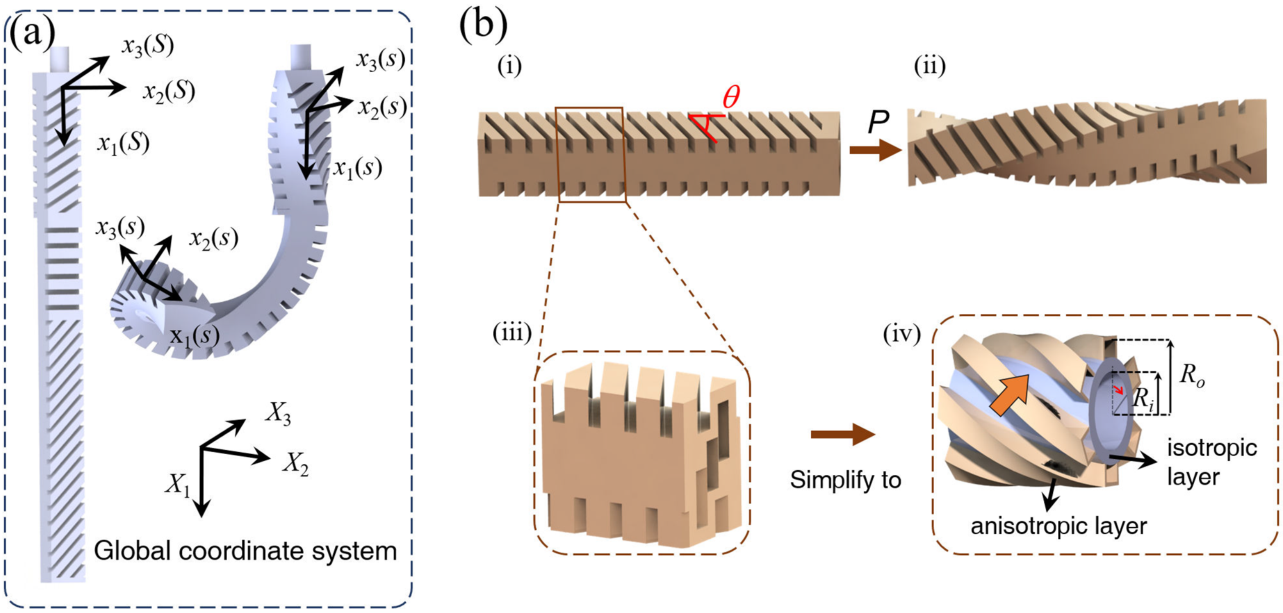

FIG. 2. The theoretical models of the multi-segment soft manipulators. The global and local coordinate systems of the initial shape are shown in (a). The local coordinate system changes with the soft manipulator's deformation. (b) Shows the theoretical model of the twisting segment. The initial and deformed twisting segments are shown in (i) and (ii). The (iii) cross-section is simplified to (iv), consisting of an isotropic inner layer and an anisotropic outer layer.

$$W_t^{aniso} = \frac{(\sqrt{I_4} - 1)^2 E_t}{2}, \tag{3}$$

where $I_4 = \boldsymbol{FA} \cdot \boldsymbol{FA}$ is a pseudo-invariant to characterize the anisotropy generated by the aligned chambers. $\boldsymbol{A} = (\cos\theta, \sin\theta, 0)$ is the direction of the chambers in the undeformed configuration. E_t represents the effective modulus of the chamber area, as hollow areas exist. The elastic energy density function of the twisting segment is then

$$\begin{aligned} W_t &= c_1 W_t^{iso} + c_2 W_t^{aniso} \\ &= c_1 \frac{\mu}{2}(I_1 - 3) + c_2 \frac{(\sqrt{I_4} - 1)^2 E_t}{2}. \end{aligned} \tag{4}$$

2. Modeling extension, expansion, and twist

When the twisting segment is inflated, a pressure P is applied on its inner surface and the outer surface is assumed to be traction-free. It exhibits an extension in the length direction and expansion in the radial direction, besides the twisting deformation. We denote the stretch in length direction and radial directions as λ_ψ and λ_z, respectively. The twisting per unit length is τ. The reference and deformed cylindrical coordinates are denoted as (R, Ψ, Z) and (r, ψ, z), respectively. The twisting per unit length is τ. Thus, the deformation in the current configuration is

$$r = \lambda_\psi R, \quad \psi = \Psi + \tau\lambda_z Z, \quad z = \lambda_z Z. \tag{5}$$

According to the incompressible constraint,

$$\pi(r_o^2 - r_i^2)l = \pi\lambda_\psi^2(R_o^2 - R_i^2)\lambda_z L = \pi(R_o^2 - R_i^2)L, \tag{6}$$

where r_i and r_o are the inner and outer positions after the deformation. L and l are the length before and after deformation. The relationship between λ_ψ and λ_z can be obtained as $\lambda_\psi^2 = 1/\lambda_z$. The deformation gradient $\boldsymbol{F}$ now takes the following form:

$$\boldsymbol{F} = \begin{pmatrix} \frac{\partial r}{\partial R} & \frac{1}{R}\frac{\partial r}{\partial \Psi} & \frac{\partial r}{\partial Z} \\ r\frac{\partial \psi}{\partial R} & \frac{r}{R}\frac{\partial \psi}{\partial \Psi} & r\frac{\partial \psi}{\partial Z} \\ \frac{\partial z}{\partial R} & \frac{1}{R}\frac{\partial z}{\partial \Psi} & \frac{\partial z}{\partial Z} \end{pmatrix} = \begin{pmatrix} \frac{R}{r\lambda_z} & 0 & 0 \\ 0 & \frac{r}{R} & r\tau\lambda_z \\ 0 & 0 & \lambda_z \end{pmatrix}. \tag{7}$$

The Cauchy stresses can be obtained as[42]

$$\boldsymbol{\sigma} = 2\frac{\partial W_t}{\partial I_1}\boldsymbol{FF}^T + 2\frac{\partial W_t}{\partial I_4}\boldsymbol{FA} \otimes \boldsymbol{FA} - p\boldsymbol{I}, \tag{8}$$

where $\boldsymbol{I}$ is the identity matrix and p is a Lagrange multiplier to ensure incompressibility. The Cauchy stress can be written explicitly as

$$\boldsymbol{\sigma} = \begin{pmatrix} \sigma_{rr} & 0 & 0 \\ 0 & \sigma_{\psi\psi} & \sigma_{\psi z} \\ 0 & \sigma_{z\psi} & \sigma_{zz} \end{pmatrix}, \tag{9}$$

where

$$\sigma_{rr} = -P + \frac{c_1\mu}{\lambda_z^2\lambda_\psi^2}, \tag{10}$$

$$\sigma_{\psi\psi} = -P + c_1(\gamma^2\lambda_z^2)\mu + \frac{c_2 E\left(-1 + \sqrt{I_4}\right)(\lambda_\psi\cos\theta + \gamma\lambda_z\sin\theta)^2}{\sqrt{I_4}}, \tag{11}$$

$$\sigma_{zz} = -P + c_1\lambda_z^2\mu + \frac{c_2 E\left(-1 + \sqrt{I_4}\right)\lambda_z^2\sin^2\theta}{\sqrt{I_4}}, \tag{12}$$

$$\sigma_{\psi z} = \sigma_{z\psi} = \lambda_z\left(c_1\gamma\lambda_z\mu + \frac{c_2 E\left(-1 + \sqrt{I_4}\right)\sin\theta(\lambda\psi\cos\theta + \gamma\lambda_z\sin\theta)}{\sqrt{I_4}}\right), \tag{13}$$

and $\gamma = \tau r$. Substituting the stresses into the following three Cauchy equilibrium equations in r, ψ, and z directions,[42]

$$\frac{\partial\sigma_{rr}}{\partial r} + \frac{1}{r}\frac{\partial\sigma_{r\psi}}{\partial\psi} + \frac{\partial\sigma_{rz}}{\partial z} + \frac{1}{r}(\sigma_{rr} - \sigma_{\psi\psi}) = 0, \tag{14}$$

$$\frac{\partial\sigma_{r\psi}}{\partial r} + \frac{1}{r}\frac{\partial\sigma_{\psi\psi}}{\partial\psi} + \frac{\partial\sigma_{\psi z}}{\partial z} + \frac{2}{r}\sigma_{r\psi} = 0, \tag{15}$$

$$\frac{\partial\sigma_{rz}}{\partial r} + \frac{1}{r}\frac{\partial\sigma_{\psi z}}{\partial\psi} + \frac{\partial\sigma_{zz}}{\partial z} + \frac{1}{r}\sigma_{rz} = 0, \tag{16}$$

we can obtain one non-vanishing equation,

$$\frac{d\sigma_{rr}}{dr} = \frac{\sigma_{\psi\psi} - \sigma_{rr}}{r}. \tag{17}$$

The following three boundary conditions are used. (BC1) The stress difference between the outer and inner surface is P, i.e.,

$$P = \sigma_{rr}(r = r_o) - \sigma_{rr}(r = r_i), \tag{18}$$

where $\sigma_{rr}(r = r_o) = 0$ and $\sigma_{rr}(r = r_i) = -P$. $\sigma_{rr}(r = r_i)$ is negative as the positive direction of normal stress points away from the surface.

Substituting Eq. (17) into Eq. (18) yields

$$P = \int_{r_i}^{r_o} \frac{\sigma_{\psi\psi} - \sigma_{rr}}{r} dr. \tag{19}$$

(BC2) The axial load is N:

$$N = 2\pi\int_{r_i}^{r_o} \sigma_{zz} \times r dr = P\pi r_i^2. \tag{20}$$

(BC3) The axial moment $M = 0$ as the twisting segment is symmetric about the length axis,

$$M = 2\pi\int_{r_i}^{r_o} \sigma_{\psi z} \times r^2 dr = 0. \tag{21}$$

By substituting Eqs. (9)–(13) into the three boundary conditions Eqs. (19)–(21), the three parameters τ, λ_z, and p can be solved numerically using function "fsolve" in Matlab. The deformed length of the tube is obtained as $l = \lambda_z L$. The twisting per unit length is τ. The expansion in the radial direction is $r = \lambda_\psi R = \sqrt{1/\lambda_z}R$.

B. Reconstruction of the 3D shapes

The deformed 3D shape of the multi-segment soft manipulator is reconstructed based on the twisting related parameter τ and λ_z, and the bending-related parameters. Though two different models are used for the twisting and helical/bending segments due to the differences in geometry and deformation patterns, both models are physical-based. The inputs are geometric, material, and loading parameters, while the outputs are the corresponding deformed shapes, including the centerline and 3D shapes. Therefore, the deformed shapes of both the twisting and helical/bending segments can be joined together using the theoretical method by ensuring continuity at their interfaces.

We first construct the centerline in the global coordinates. The 3D volume structure is then built by projecting the centerline in the width and thickness. The coordinate vector of the centerline $\boldsymbol{P}^{(i)}(s)$ for ith segment can be written as

$$\boldsymbol{P}^{(i)}(s) = P_1{}^{(i)}(s)\boldsymbol{X}_1 + P_2{}^{(i)}(s)\boldsymbol{X}_2 + P_3^{(i)}(s)\boldsymbol{X}_3, \tag{22}$$

where $P_1^{(i)}(s)$, $P_2^{(i)}(s)$, $P_3^{(i)}(s)$ are the coordinates in $\boldsymbol{X}_1$, $\boldsymbol{X}_2$, $\boldsymbol{X}_3$ axes, respectively.

In the following, the deformed shapes of the twisting segments are derived. The reconstruction of the deformed shapes of the helical segments is given in Sec. I of the SI. The rotation matrices of each segment are obtained, and the final deformation of the multi-segment soft manipulator is then reconstructed.

1. Reconstruction of the twisting segment

For a twisting segment, the segment is uniformly extended to length $l = \lambda_z L$ and the $\boldsymbol{x}_3$ plane is rotated by angle per unit length τ. Thus, $\boldsymbol{x}_3$ remains the same, while $\boldsymbol{x}_1$ and $\boldsymbol{x}_2$ rotate by an angle per unit length τ in the $\boldsymbol{x}_1$-$\boldsymbol{x}_2$ plane. The rotation matrix $\boldsymbol{R}$ is

$$\boldsymbol{R} = \begin{pmatrix} 1 & 0 & 0 \\ 0 & \cos\tau & \sin\tau \\ 0 & -\sin\tau & \cos\tau \end{pmatrix}. \tag{23}$$

2. Reconstruction of the multi-segment soft manipulators

The centerline of a multi-segment soft manipulator can be described by each segment joint together, with the length, width, and height directions change continuously at the interface. Therefore, each segment except the first one needs to be transformed by a rotation matrix. We denote the transformation matrix between the beginning and end orientations of ith segment as $\boldsymbol{R}^{(i)}$. The final coordinates of ith segment are then

$$\text{for } i = 1, \quad \boldsymbol{P}_{final}^{(1)}(s) = \boldsymbol{P}^{(1)}(s), \tag{24}$$

$$\text{for } i = 2, \quad \boldsymbol{P}_{final}^{(2)}(s) = \boldsymbol{R}^{(1)}\boldsymbol{P}^{(2)}(s) + \boldsymbol{P}_{final}^{(1)}(l^{(1)}), \tag{25}$$

$$\text{for } i = n, \quad \boldsymbol{P}_{final}^{(n)}(s) = \prod_{i=1}^{n-1}\boldsymbol{R}^{(i)}\boldsymbol{P}^{(n)}(s) + \boldsymbol{P}_{final}^{(n-1)}(l^{(n-1)}). \tag{26}$$

Using the above rule, the centerline of the 3D shapes of the multi-segment soft manipulator is reconstructed. By mapping the points on the centerline along the width and length direction, the final deformed shape can be built. We use ParaView to plot the 3D shape of the multi-segment soft manipulator. Details can be found in Sec. V of the SI.

III. VALIDATION OF THE THEORETICAL MODEL

Experiments and FE simulations for twisting actuators are conducted and used to validate the theoretical predictions in this section. The fabrication and FE procedures are given in the Secs. VII and VI of the SI. The model is implemented in a MATHEMATICA code. The

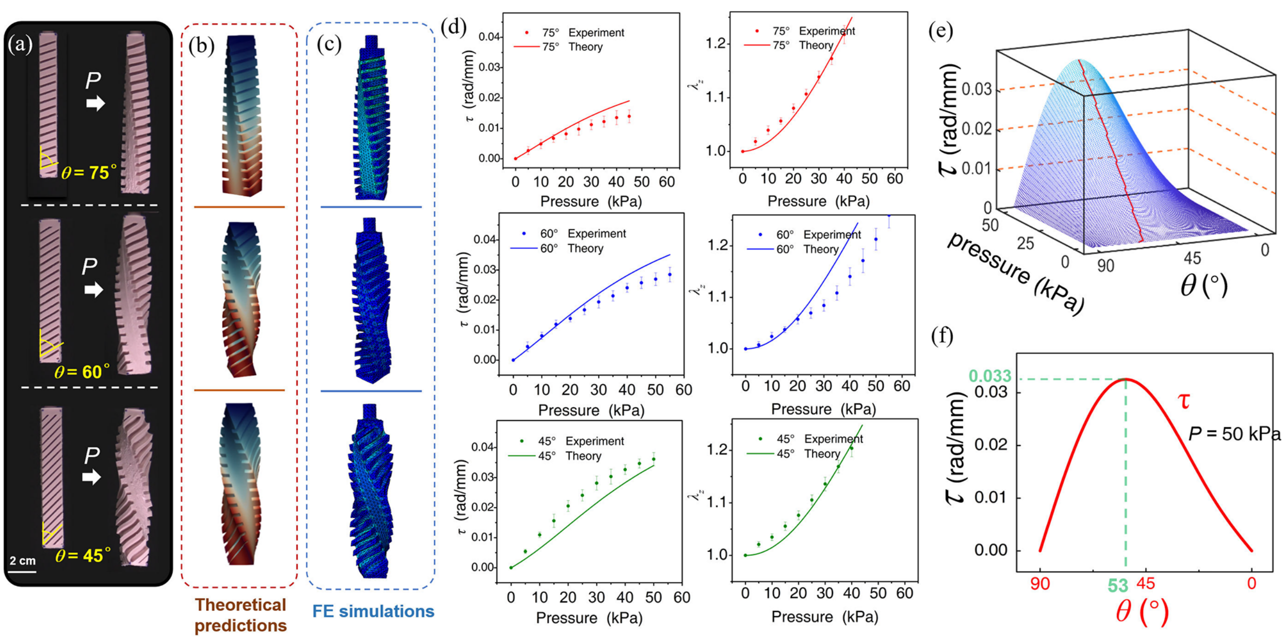

FIG. 3. Validation of the theoretical model of twisting segment. (a) The experimental initial and deformed shapes of three twisting actuators under $P = 50$ kPa with $\theta = 75^\circ, 60^\circ, 45^\circ$. The (b) theoretical predicted and (c) FE simulated deformed shapes are shown. (d) The comparison between the theoretical predicted (solid curves) and experimentally measured (markers) τ and λ_z as a function of P for the three twisting actuators. (e) The theoretical predicted 3D plot of τ as a function of P and θ. (f) The dependence of τ on θ when $P = 50$ kPa. τ reaches its maximum when $\theta =\sim 53^\circ$.

code is run on a desktop with an AMDRyzen 5 3600 central processing unit (CPU) at 3.60 GHz processor with 16GB RAM. The computation time is generally less than ten seconds.

Twisting soft actuators with $\theta = 75°$, 60°, and 45° are fabricated. Their initial and deformed experimental shapes are presented in Fig. 3(a). The applied pressure $P = 30$ kPa. It can be seen that soft actuators elongate and twist simultaneously. The corresponding theoretical and FE simulated deformed shapes are shown in Figs. 3(b) and 3(c) for comparison (SI Video 1). E_t is set as 0.008 MPa by fitting the theoretical model with the experimental τ and λ_z for all the three twisting segments with $\theta = 45°, 60°$, and 90°, as shown in Fig. 3(d). We found that the theoretical model can accurately capture all the three twisting segment's behaviors by using this parameter. The physical meaning of E_t is the effective modulus of the orthotropic layer. Once E_t is determined, it will not change for twisting soft actuators with different θ.

Next, both the twisting per unit length τ and axial elongation λ_z of the experimental and theoretical predicted deformed shapes are compared quantitatively. The theoretical predicted τ and λ_z are plotted continuously as a function of P in Fig. 3(d), while the experimentally measured values are shown as discrete points for each twisting soft actuators. Both the τ and λ_z increase with P. When P is small, the increase in τ and λ_z can be regarded as linear. However, as P increase further, τ and λ_z depends nonlinearly on P. The slope of τ decreases with P, while the slope of λ_z increases with P. The experimental and theoretical results agree well when $\theta = 75°$ and 60°, but there is some discrepancy when $\theta = 45°$, possibly due to the contact between adjacent chambers.

To further explore the dependence of the twisting on P and θ, the theoretical τ is 3D plotted in Fig. 3(e). It can be seen that (1) τ increases with P; (2) for any particular P, τ reaches its maximum at a mediate θ. The maximum τ at each P is shown by the red curve in Fig. 3(e). For example, the variation of τ with θ when $P = 50$ kPa is shown in Fig. 3(f). τ reaches its maximum value 0.033 rad/mm when $\theta = 53°$.

IV. NUMERICAL RESULTS

In this section, various multi-segment soft manipulators are designed using the validated theory. The effects of geometric parameters (segment numbers, segment combinations) and material parameters (Young's moduli) are investigated. Based on the theoretical model and the numerical results, an inverse design method is proposed. Multi-segment soft manipulators that mimic the octopus tentacle with combined twisting, bending, and helical motion are designed.

A. Effects of segment numbers

Four helical soft manipulators are designed with the same total length $L = 240$ mm as shown in Fig. 4(a). Soft manipulator (i) has one single helical segment with $\theta = 75°$. Soft manipulator (ii) is a two-segment soft manipulator with $\theta^{(1)} = 90°$, $\theta^{(2)} = 75°$, $L^{(1)} = L^{(2)} = L/2$. In the three-segment soft manipulator (iii), $\theta^{(1)} = 75°$, $\theta^{(2)} = 60°$, $\theta^{(3)} = 90°$, $L^{(1)} = L^{(2)} = L^{(3)} = L/3$. In soft manipulator (iv), $\theta^{(1)} = 75°$, $\theta^{(2)} = 60°$, $\theta^{(3)} = 45°$, $\theta^{(4)} = 90°$, $L^{(1)} = L^{(2)} = L^{(3)} = L^{(4)} = L/4$.

The deformed shapes of the four soft manipulators under different $P = 10$–50 kPa are shown in Fig. 4(b). By varying the number of segments, various shapes can be formed. Unlike the helical deformation with constant curvature formed by soft manipulator (i), shapes

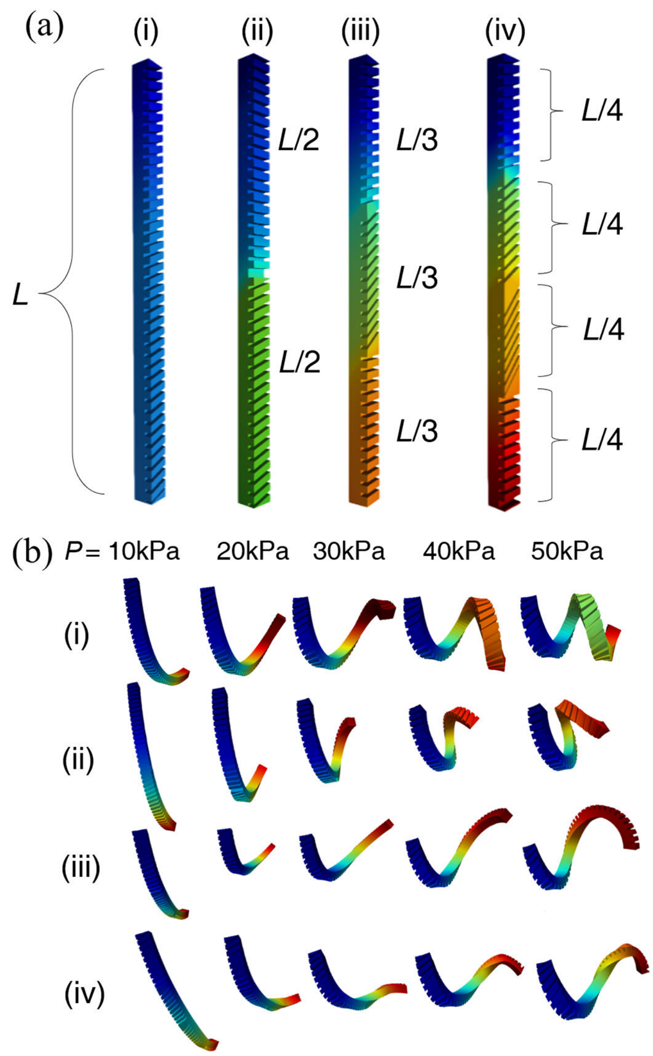

FIG. 4. Design of multi-segment soft manipulators by varying the segment numbers. (a) Four different designs of multi-segment soft manipulators. The soft manipulators have 1, 2, 3, and 4 segments, respectively. (b) The deformed shapes of the four soft manipulators under $P = 10$–50 kPa. Shapes with variable curvatures can be realized.

with variable curvatures can be constructed using multiple segments. Thus, the use of multiple segments significantly increases the workspace of soft manipulators.

B. Effects of segment combinations

Three two-segment helical soft manipulators are designed in Fig. 5 with the following parameters: 90° + 75°, 90° + 60°, and 45° + 75°, where the former number represents $\theta^{(1)}$ and the latter one represents $\theta^{(2)}$. Each segment has the same length 90 mm. Other geometrical parameters are the same as those used in the experiments. The deformed shapes at $P = 10$–50 kPa are presented. By adjusting the orientation angles in each segment, the two-segment soft manipulators' trajectory can be programmed, which can be exploited in areas, such

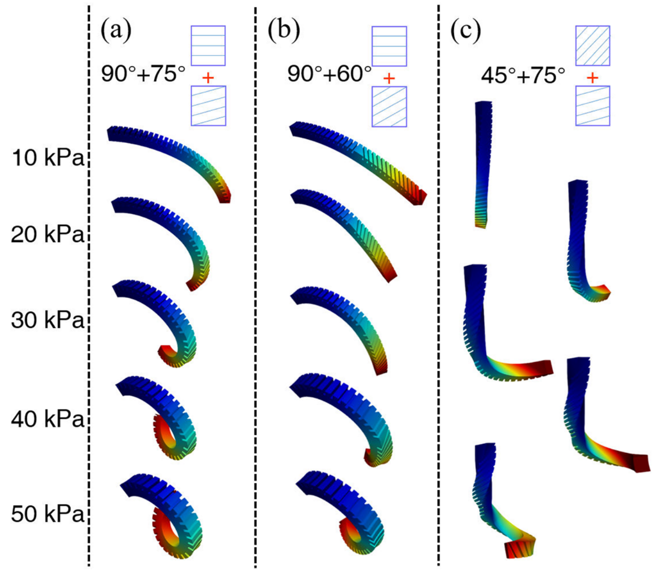

FIG. 5. Design of two-segment soft manipulators with different combination of orientation angles. Three two-segment soft manipulators are designed with (a) $\theta^{(1)} = 90°$ and $\theta^{(2)} = 75°$, (b) $\theta^{(1)} = 90°$ and $\theta^{(2)} = 60°$, (c) $\theta^{(1)} = 45°$, and $\theta^{(2)} = 75°$ The deformed shapes of the three soft manipulators under $P = 10$–50 kPa are shown. By varying the orientation angles, the trajectories can be programmed.

as grasping objects with different geometry and exploring unstructured environments.

C. Effect of Young's modulus

As the theoretical model establishes the relationship between the input loading and the deformed shapes via the material's constitutive equation, it can be applied to study the effect of the material properties on the motion of the multi-segment soft manipulators.

In Figs. 6(a) and 6(b), two three-segment helical soft manipulators are designed with (a) $\theta^{(1)} = 60°$, $\theta^{(2)} = 90°$, $\theta^{(3)} = 60°$, $L^{(1)} = L^{(3)} = 0.04$ m, $L^{(2)} = 0.07$ m and (b) $\theta^{(1)} = 45°$, $\theta^{(2)} = 90°$, $\theta^{(3)} = 75°$, $L^{(1)} = L^{(2)} = 0.06$ m, $L^{(3)} = 0.04$ m. The deformed shapes of the two three-segment soft manipulators with different Young's modulus $E = 0.8, 0.7, 0.6, 0.5$, and 0.4 MPa are shown. The applied pressure is fixed as $P = 50$ kPa. It can be seen that the deformation increases with the decrease in E at a fixed pressure.

In Fig. 6(c), the effects of different combinations of material properties are shown. The geometric parameters of the soft manipulators are the same with $\theta^{(1)} = 45°$, $\theta^{(2)} = 90°$, $\theta^{(3)} = 45°$, $L^{(1)} = L^{(3)} = 0.04$ m, $L^{(2)} = 0.06$ m. The E of each segment has different values. For soft manipulator (i), (ii), and (iii), $E_i = 0.4 + 0.4 + 0.4$ MPa, $E_{ii} = 0.4 + 0.6 + 0.4$ MPa, and $E_{iii} = 0.9 + 0.3 + 0.9$ MPa. The three values represent the E of first, second and third segments, respectively. It can be seen that by adjusting the material properties in each segment, the deformation can be tuned. For example, the second segment of soft manipulator (ii) has relatively larger E. Therefore, its bending curvature is smaller than that in the segment 2 of soft manipulator (i).

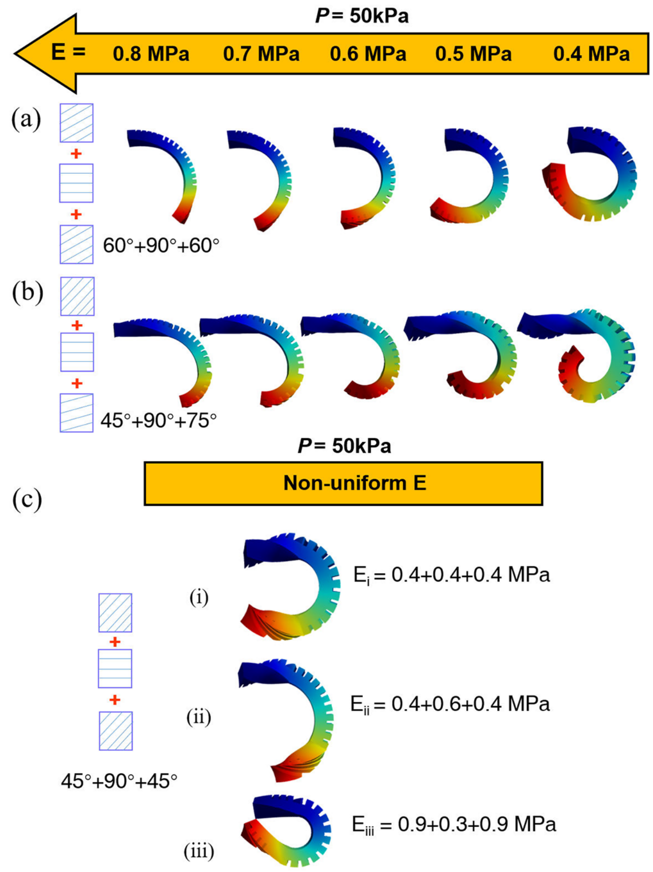

FIG. 6. Effect of Young's modulus. Two three-segment helical soft manipulators are designed with (a) $\theta^{(1)} = 60°$, $\theta^{(2)} = 90°$, $\theta^{(3)} = 60°$, $L^{(1)} = L^{(3)} = 0.04$ m, $L^{(2)} = 0.07$ m, and (b) $\theta^{(1)} = 45°$, $\theta^{(2)} = 90°$, $\theta^{(3)} = 75°$, $L^{(1)} = L^{(2)} = 0.06$ m, $L^{(3)} = 0.04$ m. The deformed shapes of the three-segment helical soft manipulators with different Young's modulus $E = 0.8$–0.4 MPa is shown. $P = 50$ kPa. (c) The geometric parameters of the three-segment helical soft manipulators are $\theta^{(1)} = 45°$, $\theta^{(2)} = 90°$, $\theta^{(3)} = 45°$, $L^{(1)} = L^{(3)} = 0.04$ m, $L^{(2)} = 0.06$ m. Three different combinations of material properties are used: (i) $0.4 + 0.4 + 0.4$ MPa, (ii) $0.4 + 0.6 + 0.4$ MPa, and (iii) $0.9 + 0.3 + 0.9$ MPa. The deformed shapes of the three soft manipulators under $P = 50$ kPa are shown.

D. Inverse design

Inspired by the octopus tentacles where a single tentacle can exhibit a combination of bending and twisting motions, the theoretical model can be used to inversely design single-input, multi-segment soft manipulators that follow specific trajectories. Soft manipulators matching the surfaces of objects can be designed and used to grasp fragile objects. Grasping fragile objects is difficult. Soft manipulators are a good choice due to their soft materials. However, to ensure perfect contact and reduce the stress concentration, the trajectories of the soft manipulators should perfectly match the surface of the fragile objects. The developed theoretical method can be used to design soft manipulators that follow these particular trajectories.

The procedures for the inverse design are as follows:

(1) the objective curve (or points) is categorized into twisting, bending, or helical segment manually, and their geometric parameters are extracted by fitting;
(2) by comparing the extracted parameters with a lookup table, we find a roughly estimated curve as the initial guess for the optimization;
(3) we use the constrained optimization method in Matlab to find the optimal design parameters.

Figure 7(a) shows the schematic trajectory of an octopus tentacle. To mimic this motion, we first discretize the tentacle's motion into three types: twisting, bending and 3D helical deformations [Fig. 7(b)]. The corresponding deformation-related geometrical parameters are extracted, including twisting per unit length τ and arc length l_t for the twisting segment, bending curvature κ_b and arc length l_b for the bending segment, and curvature κ_h, pitch P_t and arc length l_h for the helical segment.

Figure 8 illustrates the detailed procedures of extracting the geometric parameters. The twisting angle per unit length γ is easily calculated using $\gamma = \tau/L_t$, where τ is the total twisting in the twisting segment [Fig. 8(b)]. For the bending and helical segments, we first transform the points to the standard orientations along the coordinate axis using a rotation matrix that represents the rotation matrix between the tangent vector at the segment end and the coordinate axis. The transformed points can then be fitted using the standard form of the bending and helical curves [Figs. 8(c) and 8(d)]. The points in the bending segment are fitted using the form $(x - 1/\kappa_b)^2 + y^2 = (1/\kappa_b)^2$. The points in the helical segment are fitted using the form: $x(t) = a\cos(t)$, $y(t) = a\sin(t)$ and $z(t) = bt$, where $a = 1/\kappa_h$, $b = P_t/2\pi$ and t is a parameter. Using the above procedures, the geometric parameters of the spatial points/curve can be extracted.

Next, we use the lookup table to find the roughly estimated geometric, material and loading parameters for a prescribed objective curve [Fig. 8(f)]. The lookup table is established using the theoretical model proposed in this work. It should be noted that the applied

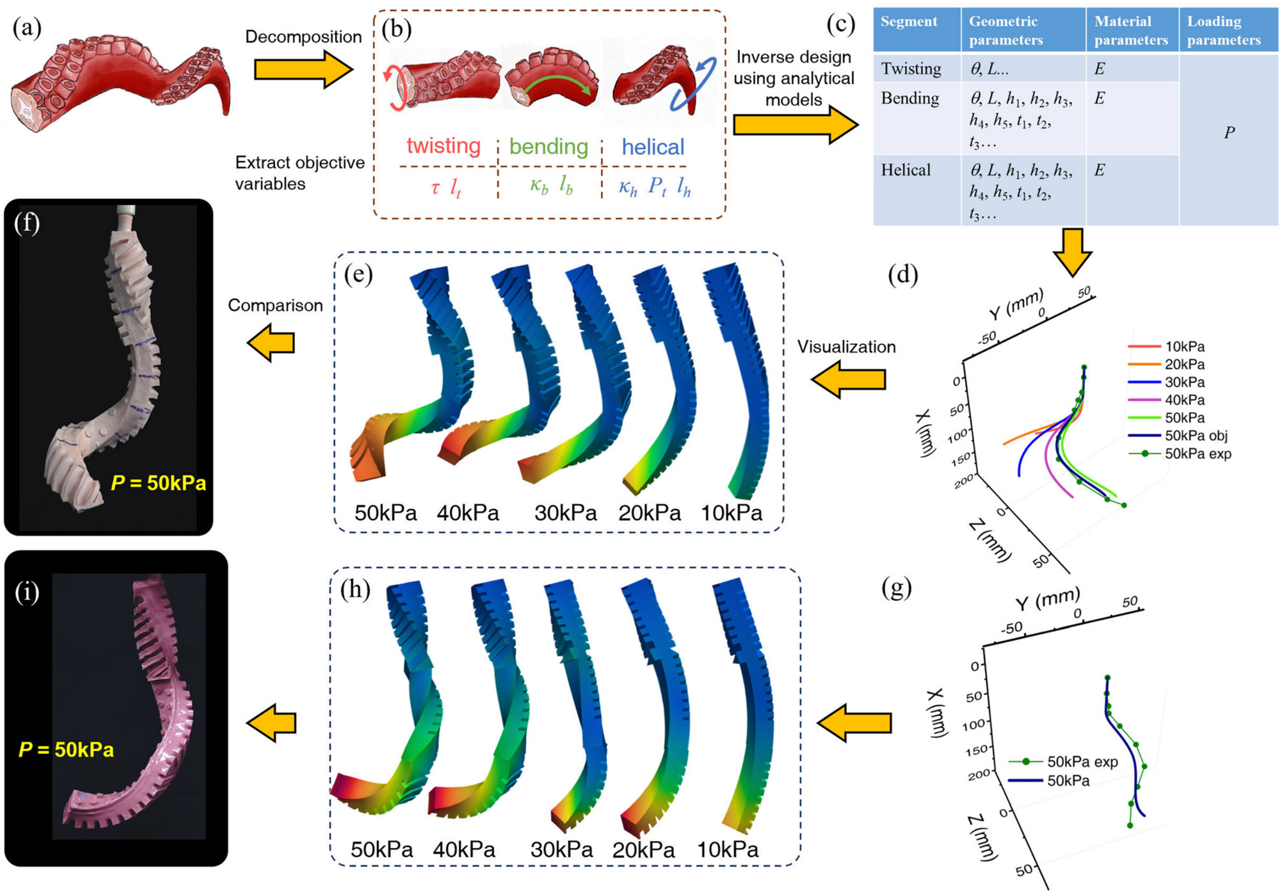

FIG. 7. Inverse design of bio-inspired multi-segment soft manipulators with trajectory matching. (a) Shows a schematic of a single tentacle that can exhibit a combination of bending and twisting motions. (b) The motions are decomposed into twisting, bending and helical deformation with prescribed objective variables. By using the theoretical model, the multi-segment soft manipulator can be inversely designed. The geometric and material parameters are obtained in (c). The theoretical trajectories of the designed soft manipulators under $P = 10$–50 kPa are shown in (d). The objective trajectory and experimental trajectory under $P = 50$ kPa are also shown. The theoretical deformed shapes of the soft manipulators under 10–50 kPa are shown in (e). The soft manipulator is fabricated using the obtained geometric and material parameters. Its deformation under $P = 50$ kPa is shown in (f). Another example of the inverse design is shown in (g), (h), and (i). The MSE (mean squared error) in (d) and (g) are 3.86×10^{-4} m^2 and 1.83×10^{-3} m^2, respectively.

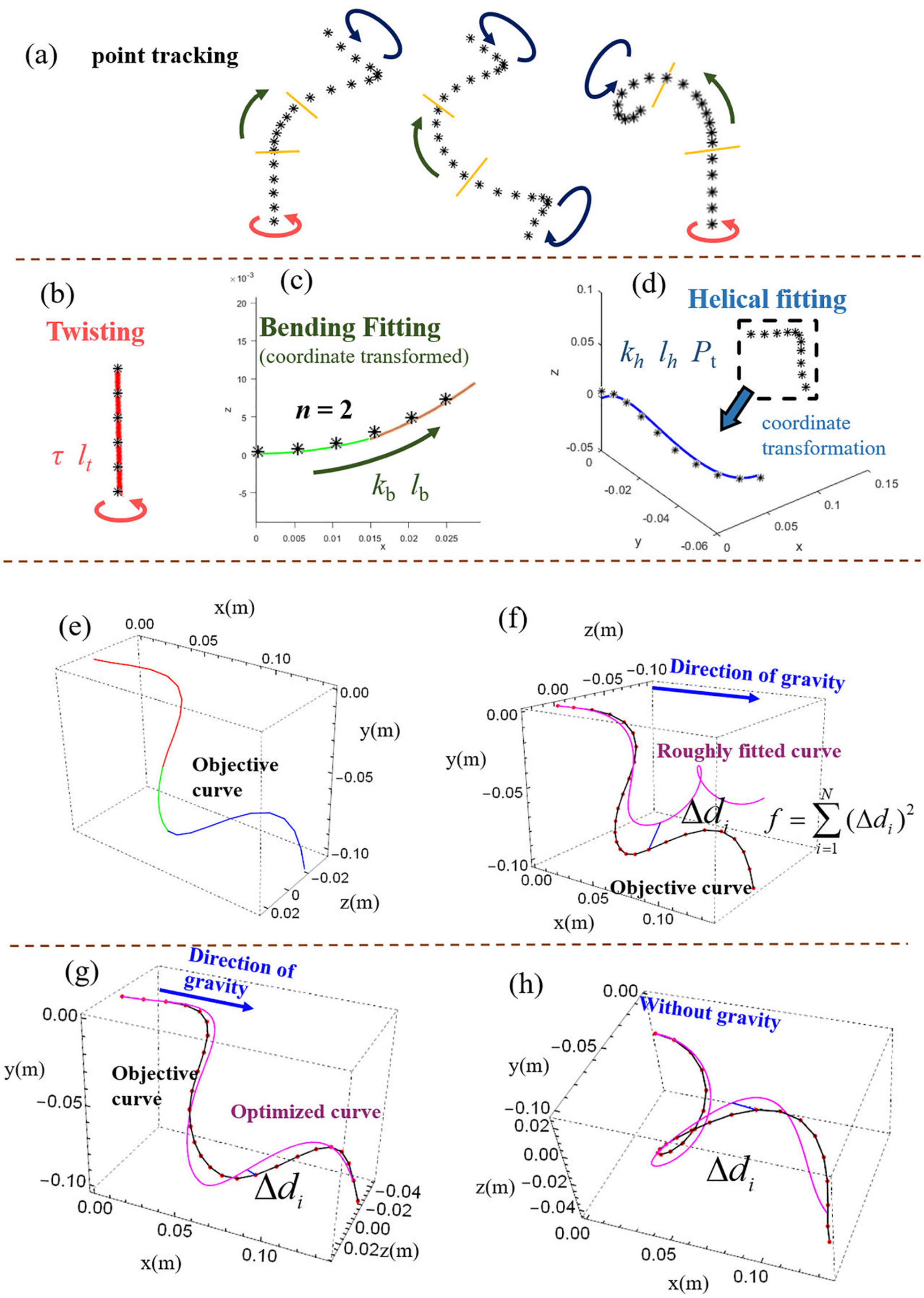

FIG. 8. The procedures for identifying the geometric parameters for a target 3D curve. (a) A target 3D curve is split into several segments which display twisting, bending or helical deformation separately. The red, green, and blue arrows represent twisting, bending, and helical segments, respectively. (b), (c), and (d) The geometric parameters related to the twisting, bending, and helical segments are identified. Another example showing the optimization procedures. (e) Shows the objective curve. (f) Shows the roughly fitted curves using the lookup table method. Δd_i is the minimum distance of point i to the designed curve. (g) Shows the optimized curves with gravity considered. (h) Shows the optimized curves without gravity.

pressure is the same for all segments, as the chambers in each segment are connected.

We then use the constrained optimization method in Matlab to find the optimal design parameters, using the roughly estimated parameters as the initial guess. At each cycle, the deformed shape without gravity is calculated using the theoretical model first [Fig. 8(h)]. Next, the effect of gravity is considered to estimate the deformation of the soft manipulator [Fig. 8(g)]. Details are shown in Sec. IV in SI. The

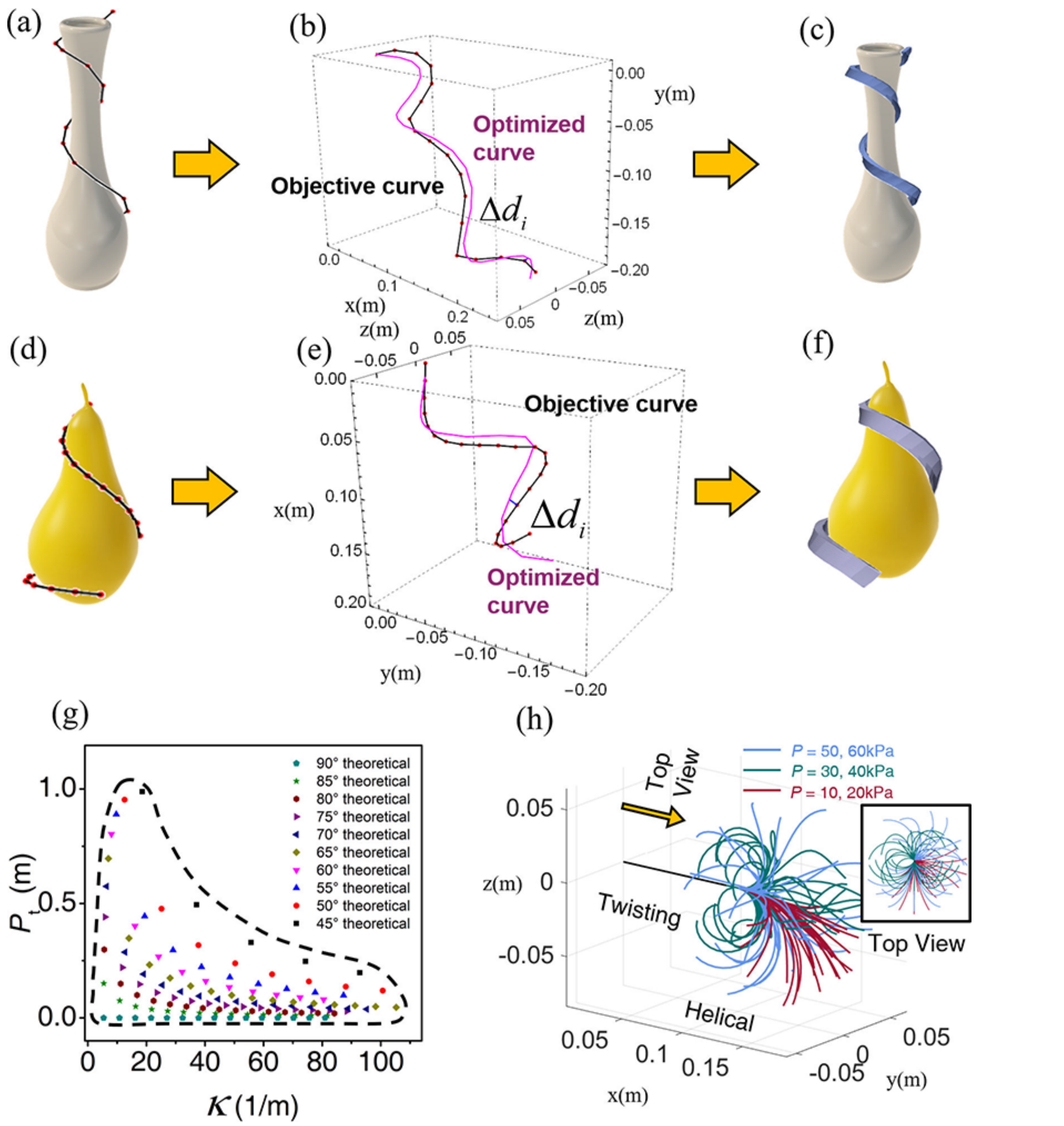

FIG. 9. Inverse design methods and workspace of soft manipulators with deformed shapes matching the surface of fragile objects. Grasping a concave vase and convex pear is demonstrated. (a) and (d) A conformal curve that wrapping the vase or the pear is obtained as the desired curves. (b) and (e) The optimized curves are calculated using the automated design tool. (c) and (f) The theoretical predicted deformed shapes on the vase. The MSEs in (b) and (e) are $2.15 \times 10^{-4}\,m^2$ and $1.91 \times 10^{-4}\,m^2$, respectively. (g) The κ and P_t distribution of the helical/bending segment. The orientation angles are from 45° to 135°, and the range of P is chosen from 0 kPa to 60 kPa. (h) The demonstrated workspace of the two-segment soft manipulator. At each P, 14 curves with $\theta = 45°–135°$ are plotted. The curves under different pressures are denoted by different colors. Red: 10 kPa and 20 kPa. Green: 30 kPa and 40 kPa. Blue: 50 kPa and 60 kPa.

objective function is defined as the summation of the distance square between the objective points to the theoretically calculated curve,

$$f = \sum_{i=1}^{N} (\Delta d_i)^2, \tag{27}$$

where N is the number of the objective points and Δd_i is the minimum distance of point i to the theoretically calculated curve. The "fmincon" function in Matlab is used. Parameters H_2, H_3, and P are varied to find the optimal parameters. The constrained ranges used in Fig. 8 are $0.6P_e < P < 1.4P_e$, $1\,\mathrm{mm} < H_2 < 3\,\mathrm{mm}$ and $4\,\mathrm{mm} < H_3 < 6\,\mathrm{mm}$, where P_e is the roughly estimated applied pressure. If the minimum f is found at the range's boundary, we then vary more parameters or expand the ranges until a local minimum f is found inside the boundaries.

Experiments are also conducted to validate the inverse design method, as shown by Fig. 7(d) and Fig. 7(i). In this case, the prescribed objective variables are set as $\tau = 0.01\pi$ rad/mm, $l_t = 0.05$ m, $\kappa = 18\,\mathrm{m}^{-1}$, $l_b = 0.03$ m, $\kappa = 70\,\mathrm{m}^{-1}$ $P_t = 0.09$ m, and $l_h = 0.1$ m. The trajectories of the centerlines of the designed multi-segment soft manipulator under various pressure $P = 10$–50 kPa are shown in Fig. 7(d). The objective trajectory is shown by the blue curve for comparison. The theoretical predicted 3D shapes of the designed soft manipulator under $P = 10$–50 kPa are shown in Fig. 7(e). The designed soft manipulators are fabricated using the exact calculated geometric parameters and materials. Its deformed shape is shown in Fig. 7(f) (SI Video 3). The experimental trajectory is also shown in Fig. 7(d). The mean squared error (MSE) between the objective and experimental centerlines is $3.86 \times 10^{-4}\,\mathrm{m}^2$.

Use the same design method, we design another multi-segment soft manipulator (SI Video 3). The objective curve is shown in Fig. 7(g). To obtain the same trajectory, a three-segment soft manipulator is designed. The first segment is a twisting segment with $\theta = 60°$, and the orientation angles of the second and third segment are $-45°$ and $60°$, respectively. The theoretical predicted shapes at different $P = 10$–50 kPa are shown in Fig. 7(h). The experiment shape of the fabricated soft manipulator under $P = 50$ kPa is shown in Fig. 7(i).

The geometric parameters, such as the orientation angles and inner chamber geometries, are obtained as shown in Table II in Sec. III of the SI. In the calculation, the input pressure is set as $P = 50$ kPa. We use the same material for all the segments in the inverse design to facilitate the sequencing fabrication. Gravity is considered.

Two examples of soft manipulators matching object surfaces are shown in Fig. 9. One is a vase, and the other one is a pear. The vase has a concave surface, while the pear has a convex surface. First, an objective curve is constructed, which matches the vase or the pear surface, as shown in Figs. 9(a) and 9(d). Next, the optimized curves are calculated using the inverse design method, as shown in Figs. 9(b) and 9(e). The deformed 3D shapes are plotted on the fragile objects Figs. 9(c) and 9(f). Gravity is neglected to reduce the computational cost, and the chambers are not shown in the figure. The detailed geometric and loading parameters are shown below. For the vase curve, three segments of orientation angles $\theta^{(1)} = 70°$, $\theta^{(2)} = 55°$, and $\theta^{(3)} = 70°$ are used, and the final pressure $P = 36.4$ kPa. Two segments with $\theta^{(1)} = 70°$, $\theta^{(2)} = 55°$ are used to fit the pear surface and the pressure $P = 42.6$ kPa. The other geometric parameters used are $h_1 = 3.5$ mm, $h_2 = 2.0$ mm, $h_3 = 7.0$ mm, $h_4 = 2.0$ mm, $h_5 = 4.0$ mm, $t_1 = 1.0$ mm, $t_2 = 1.0$ mm, and $t_3 = 1.0$ mm. The material parameters are $E = 0.619$ MPa and $\nu = 0.49$.

It should be noted that the model cannot recreate any arbitrary curve due to the geometric, material and loading restrictions. For example, for ease of fabrication, the thickness of the silicone layer is generally between 1.0 and 2.0 mm. The elastic modulus of the silicone rubber is in the range of 0.1–1 MPa by varying the combinations of the base and curing agents. The loading pressure should be smaller than 60 kPa to avoid leaking. These restrictions on the parameters will limit the performance ranges of the designed curves.

To obtain the workspace of the multi-segment soft manipulators, the workspace for the twisting and helical/bending segments are estimated separately first. To ease the calculation, we focus only on the variation of the orientation angle θ and pressure P. The range of other parameters is relatively small. For a twisting segment, the twising τ as a function of θ and pressure P are plotted in Fig. 3(e). Under a particular P, the range of τ for all kinds of θ can be obtained. For example, at $P = 10$ kPa, the range of τ is 0–0.0063 rad/mm. At $P = 50$ kPa, τ varies from 0 rad/mm to 0.0325 rad/mm.

Next, the workspace of the helical/bending segment is estimated. Similar to the twisting segment, we only vary θ and P for the helical/bending segment. Figure 9(g) plots the κ and P_t distribution of the helical/bending segment. The orientation angles are from 45° to 90° with 5° interval, and P varies from 0 kPa to 60 kPa. It can be seen that not all κ and P_t combinations can be realized. The dotted curves represent the covered range.

To quantitatively estimate the workspace of the multi-segment soft manipulator, we take a two-segment soft manipulator as an example. The first segment is denoted as a twisting segment, while the second segment is a helical/bending segment. Figure 9(h) plots the workspace of the designed soft manipulators. P is the same for both segments as the chambers are connected and varies from 0 kPa to 60 kPa. 14 curves are plotted at each P to show the corresponding workspace and are labeled by different colors. θ varies from 0° to 90° for the twisting segments, and varies from 45° to 135° for the helical/bending segments. The other geometric parameters used are $h_1 = 3.5$ mm, $h_2 = 2.0$ mm, $h_3 = 7.0$ mm, $h_4 = 2.0$ mm, $h_5 = 4.0$ mm, $t_1 = 1.0$ mm, $t_2 = 1.0$ mm, and $t_3 = 1.0$ mm. The material parameters are $E = 0.619$ MPa and $\nu = 0.49$. The workspace for soft manipulators with the different segment or segment combinations can be obtained using similar procedures.

V. CONCLUSION

This work presents a multi-segment soft manipulator that can match a specific trajectory in 3D space under a single input pressure. The soft manipulator consists of multiple segments, and each segment demonstrates twisting, bending, or 3D helical deformation resulting from its geometrical design. To inverse design the spatial trajectories, a theoretical framework is proposed. The theoretical framework establishes the relationship between the input pressure and the final trajectories via the material's constitutive equation. An orthotropic nonlinear energy density function is used to describe the twisting segment. By solving the Cauchy equilibrium equations in a cylindrical coordinate, the twisting, expansion, and elongation of the twisting segment under input pressure are obtained. As the loading direction varies when the helical segment deforms in 3D space, a minimum potential energy method is employed to model the helical segment. By using a 3D rod theory, the trajectory of the multi-segment soft manipulator is established. A method is then developed to visualize the 3D deformed shapes of the multi-segment soft manipulators. Experiments and FE simulation are conducted to validate the theoretical model. The computational cost of the theoretical model is significantly lower than that using the FE method. By virtue of the low computational cost of the theoretical model, the effects of geometric and material properties and segment combinations are studied. Various inverse designs of the multi-segment soft manipulators' trajectories are presented.

Future works are needed to achieve truly versatile applications of the designed soft manipulators. Using the developed design tool, future work can generalize the developed strategies to systems with multiple actuators, which may find real world applications in seafood animals collections, vegetables and fruits harvesting, soft prosthesis, etc. Developing a dynamic model for the soft manipulator is also necessary. Modeling contact and the design of multiple actuators with hyper-redundancy are also existing challenges. Moreover, the current inverse design process is not entirely automatic, as the first stage is a human picking the regions of a curve and assigning it to either twisting, bending, or helical deformation. The prospect of implementing an automated system to do this step using machine learning or cost function methods is discussed in Sec. II in SI.

The major contributions and findings can be summarized as follows. First, we propose the design of a pneu-net twisting segment and develop a nonlinear model to describe its actuation. Theoretical predictions show that the twisting is maximized when $\theta =\sim 53^{\circ}$.

Second, we extend the theoretical model based on the minimum potential energy for a single helical segment to multiple helical segment. Compared to the previous soft manipulators with a single orientation angle, the workspace is significantly expanded by varying the number and the orientation angle of each segment.

Third, a 3D rod theory is employed to reconstruct the shape of the soft manipulator, which accounts for the coordinate transformation and manipulator's elongation.

Fourth, the constitutive model relates the input parameters, including the material, geometric, and loading parameters, directly to the final deformation. Thus, it can be used to program the shape change under actuation by adjusting the input parameters. Numerical results show that the deformed shape can be programmed by tuning the segment number, orientation angles, material stiffness in each segment, etc.

Finally, an inverse design method is proposed to design the soft manipulators' spatial trajectories. Multi-segment soft manipulators that mimic the twisting, bending, and 3D helical deformations of the octopus tentacles are designed. Soft manipulators matching the surface of fragile objects are designed. The proposed design method has immense potential to design soft manipulators for particular tasks in 3D space and to broaden their applications.

SUPPLEMENTARY MATERIAL

See the supplementary material for more information that supports the findings of this study, including the theoretical model of the multiple helical segments, optimization procedures, visualization procedures, finite element methods, experimental details, and videos.

ACKNOWLEDGMENTS

D.W. acknowledges the support from the National Natural Science Foundation of China (Grant No. 51905336) and the Shanghai Sailing Program (Grant No. 19YF1423000). G.Y. acknowledges the support from the National Natural Science Foundation of China (Grant No. 52025057).

AUTHOR DECLARATIONS

Conflict of Interest

The authors have no conflicts to disclose.

DATA AVAILABILITY

The data that support the findings of this study are available from the corresponding authors upon reasonable request.

REFERENCES

[1] V. Magdanz, J. Gebauer, D. Mahdy, J. Simmchen, and I. S. Khalil, "Sperm-templated magnetic microrobots," in *International Conference on Manipulation, Automation and Robotics at Small Scales (MARSS)* (IEEE, 2019), pp. 1–6.
[2] M. Wang, B.-P. Lin, and H. Yang, "A plant tendril mimic soft actuator with phototunable bending and chiral twisting motion modes," Nat. Commun. **7**, 13981 (2016).
[3] M. Schaffner, J. A. Faber, L. Pianegonda, P. A. Rühs, F. Coulter, and A. R. Studart, "3D printing of robotic soft actuators with programmable bioinspired architectures," Nat. Commun. **9**, 878 (2018).
[4] W. Hu and G. Alici, "Bioinspired three-dimensional-printed helical soft pneumatic actuators and their characterization," Soft Rob. **7**, 267–282 (2020).
[5] N. K. Uppalapati and G. Krishnan, "Towards pneumatic spiral grippers: Modeling and design considerations," Soft Rob. **5**, 695–709 (2018).
[6] T. T. Hoang, P. T. Phan, M. T. Thai, N. H. Lovell, and T. N. Do, "Bio-inspired conformable and helical soft fabric gripper with variable stiffness and touch sensing," Adv. Mater. Technol. **5**(12), 2000724 (2020).
[7] W. Wang, C. Li, M. Cho, and S.-H. Ahn, "Soft tendril-inspired grippers: Shape morphing of programmable polymer-paper bilayer composites," ACS Appl. Mater. Interfaces **10**, 10419–10427 (2018).
[8] S. Gong and W. Cheng, "Toward soft skin-like wearable and implantable energy devices," Adv. Energy Mater. **7**, 1700648 (2017).
[9] C. Laschi, B. Mazzolai, and M. Cianchetti, "Soft robotics: Technologies and systems pushing the boundaries of robot abilities," Sci. Rob. **1**, eaah3690 (2016).
[10] S. Xu, D. M. Vogt, W. Hsu, J. Osborne, T. Walsh, J. R. Foster, S. K. Sullivan, V. C. Smith, A. W. Rousing, and E. C. Goldfield, "Biocompatible soft fluidic strain and force sensors for wearable devices," Adv. Funct. Mater. **29**, 1807058 (2019).
[11] Y. Mengüç, Y.-L. Park, E. Martinez-Villalpando, P. Aubin, M. Zisook, L. Stirling, R. J. Wood, and C. J. Walsh, "Soft wearable motion sensing suit for lower limb biomechanics measurements," in *IEEE International Conference on Robotics and Automation* (IEEE, 2013), pp. 5309–5316.
[12] Y. Wu, J. K. Yim, J. Liang, Z. Shao, M. Qi, J. Zhong, Z. Luo, X. Yan, M. Zhang, and X. Wang, "Insect-scale fast moving and ultrarobust soft robot," Sci. Rob. **4**, eaax1594 (2019).
[13] J. Cao, L. Qin, J. Liu, Q. Ren, C. C. Foo, H. Wang, H. P. Lee, and J. Zhu, "Untethered soft robot capable of stable locomotion using soft electrostatic actuators," Extreme Mech. Lett. **21**, 9–16 (2018).
[14] C. Majidi, "Soft robotics: A perspective-current trends and prospects for the future," Soft Rob. **1**, 5–11 (2014).
[15] Y. Hao, Z. Gong, Z. Xie, S. Guan, X. Yang, Z. Ren, T. Wang, and L. Wen, "Universal soft pneumatic robotic gripper with variable effective length," in *35th Chinese Control Conference (CCC)* (IEEE, 2016), pp. 6109–6114.
[16] Y. Li and M. Hashimoto, "Design and prototyping of a novel lightweight walking assist wear using PVC gel soft actuators," Sens. Actuators A Phys. **239**, 26–44 (2016).

[17]C.-P. Chou and B. Hannaford, "Measurement and modeling of McKibben pneumatic artificial muscles," IEEE Trans. Rob. Autom. **12**, 90–102 (1996).
[18]B. Tondu and P. Lopez, "Modeling and control of McKibben artificial muscle robot actuators," IEEE Control Syst. Mag. **20**, 15–38 (2000).
[19]S. D. Thomalla and J. D. Van de Ven, "Modeling and implementation of the McKibben actuator in hydraulic systems," IEEE Trans. Rob. **34**, 1593–1602 (2018).
[20]G. Gu, D. Wang, L. Ge, and X. Zhu, "Analytical modeling and design of generalized pneu-net soft actuators with three-dimensional deformations," Soft Rob. **8**, 462–477 (2020).
[21]J. Jung, M. Park, D. Kim, and Y.-L. Park, "Optically sensorized elastomer air chamber for proprioceptive sensing of soft pneumatic actuators," IEEE Rob. Autom. Lett. **5**, 2333–2340 (2020).
[22]F. Ilievski, A. D. Mazzeo, R. F. Shepherd, X. Chen, and G. M. Whitesides, "Soft robotics for chemists," Angew. Chem. **123**, 1930–1935 (2011).
[23]R. V. Martinez, J. L. Branch, C. R. Fish, L. Jin, R. F. Shepherd, R. M. Nunes, Z. Suo, and G. M. Whitesides, "Robotic tentacles with three-dimensional mobility based on flexible elastomers," Adv. Mater. **25**, 205–212 (2013).
[24]R. F. Shepherd, F. Ilievski, W. Choi, S. A. Morin, A. A. Stokes, A. D. Mazzeo, X. Chen, M. Wang, and G. M. Whitesides, "Multigait soft robot," Proc. Natl. Acad. Sci. **108**, 20400–20403 (2011).
[25]M. T. Tolley, R. F. Shepherd, B. Mosadegh, K. C. Galloway, M. Wehner, M. Karpelson, R. J. Wood, and G. M. Whitesides, "A resilient, untethered soft robot," Soft Rob. **1**, 213–223 (2014).
[26]R. F. Shepherd, A. A. Stokes, J. Freake, J. Barber, P. W. Snyder, A. D. Mazzeo, L. Cademartiri, S. A. Morin, and G. M. Whitesides, "Using explosions to power a soft robot," Angew. Chem. Int. Ed. **52**, 2892–2896 (2013).
[27]P. Polygerinos, S. Lyne, Z. Wang, L. F. Nicolini, B. Mosadegh, G. M. Whitesides, and C. J. Walsh, "Towards a soft pneumatic glove for hand rehabilitation," in *IEEE/RSJ International Conference on Intelligent Robots and Systems* (IEEE, 2013), pp. 1512–1517.
[28]K. M. de Payrebrune and O. M. O'Reilly, "On constitutive relations for a rod-based model of a pneu-net bending actuator," Extreme Mech. Lett. **8**, 38–46 (2016).
[29]C. Majidi, R. F. Shepherd, R. K. Kramer, G. M. Whitesides, and R. J. Wood, "Influence of surface traction on soft robot undulation," Int. J. Rob. Res. **32**, 1577–1584 (2013).
[30]P. Polygerinos, Z. Wang, J. T. Overvelde, K. C. Galloway, R. J. Wood, K. Bertoldi, and C. J. Walsh, "Modeling of soft fiber-reinforced bending actuators," IEEE Trans. Rob. **31**, 778–789 (2015).
[31]C. B. Teeple, T. N. Koutros, M. A. Graule, and R. J. Wood, "Multi-segment soft robotic fingers enable robust precision grasping," Int. J. Rob. Res. **39**(14), 1647–1667 (2020).
[32]S. Y. Kim, R. Baines, J. Booth, N. Vasios, K. Bertoldi, and R. Kramer-Bottiglio, "Reconfigurable soft body trajectories using unidirectionally stretchable composite laminae," Nat. Commun. **10**, 3464 (2019).
[33]F. Connolly, C. J. Walsh, and K. Bertoldi, "Automatic design of fiber-reinforced soft actuators for trajectory matching," Proc. Natl. Acad. Sci. **114**, 51–56 (2017).
[34]J. Bishop-Moser and S. Kota, "Design and modeling of generalized fiber-reinforced pneumatic soft actuators," IEEE Trans. Rob. **31**, 536–545 (2015).
[35]K. C. Galloway, P. Polygerinos, C. J. Walsh, and R. J. Wood, "Mechanically programmable bend radius for fiber-reinforced soft actuators," in *16th International Conference on Advanced Robotics (ICAR)* (IEEE, 2013), pp. 1–6.
[36]Z. Gong, X. Fang, X. Chen, J. Cheng, Z. Xie, J. Liu, B. Chen, H. Yang, S. Kong, and Y. Hao, "A soft manipulator for efficient delicate grasping in shallow water: Modeling, control, and real-world experiments," Int. J. Rob. Res. **40**, 449–469 (2020).
[37]F. Renda, M. Giorelli, M. Calisti, M. Cianchetti, and C. Laschi, "Dynamic model of a multibending soft robot arm driven by cables," IEEE Trans. Rob. **30**, 1109–1122 (2014).
[38]G. Runge, M. Wiese, L. Günther, and A. Raatz, "A framework for the kinematic modeling of soft material robots combining finite element analysis and piecewise constant curvature kinematics," in *3rd International Conference on Control, Automation and Robotics (ICCAR)* (IEEE, 2017), pp. 7–14.
[39]L. Ge, L. Dong, D. Wang, Q. Ge, and G. Gu, "A digital light processing 3d printer for fast and high-precision fabrication of soft pneumatic actuators," Sens. Actuators A Phys. **273**, 285–292 (2018).
[40]F. Connolly, P. Polygerinos, C. J. Walsh, and K. Bertoldi, "Mechanical programming of soft actuators by varying fiber angle," Soft Rob. **2**, 26–32 (2015).
[41]D. Drotman, S. Jadhav, M. Karimi, P. de Zonia, and M. T. Tolley, "3d printed soft actuators for a legged robot capable of navigating unstructured terrain," in *IEEE International Conference on Robotics and Automation (ICRA)* (IEEE, 2017), pp. 5532–5538.
[42]F. Kassianidis, "Boundary-value problems for transversely isotropic hyperelastic solids," Ph.D. thesis (University of Glasgow, 2007).